Creep behavior identification of an environmental barrier coating using full-field measurements

Thibaut Archer, Myriam Berny, Pierre Beauchêne, François Hild

Creep behavior identification of an environmental barrier coating using full-field measurements

Thibaut ARCHER[abc], Myriam BERNY[ac], Pierre BEAUCHÊNE[b], François HILD[c]

[a]SAFRAN Ceramics, a technology platform of Safran Tech, Mérignac, France
[b]ONERA, 29 avenue de la Division Leclerc, 92320 Châtillon, France
[c]Université Paris-Saclay, ENS Paris-Saclay, CNRS, LMT – Laboratoire de Mécanique et Technologie, Cachan, France

Abstract: For the use of thermal and environmental barrier coating (T/EBC) with ceramic matrix composites, it is crucial to master the behavior under (extreme) environments representative of the hot section of engine turbines. An experimental setup to simulate such thermal loading has been developed with various diagnostics enabling for kinematic and thermal field measurements, which are used to drive a finite element model and estimate thermomechanical properties such as creep parameters.

Keywords: Environmental barrier coating (EBC), Finite Element Model Updating (FEMU), Full-field measurements, Creep

1 Introduction

Environmental barrier coatings (EBCs) have been developed for challenging environments such as gas turbine engines to improve fuel efficiency [1], [2]. Substantial gains may still be achieved with increasing operating temperatures in the high-pressure turbine section but require new generations of materials to replace the current, internally cooled, superalloy structures. Among various candidates, ceramic matrix composites (CMCs) are currently considered as an attractive option due to their high temperature resistance and low density [3]–[5]. However, the presence of water vapor leads to rapid surface recession [6]–[8], hence the development of protective coatings not only to withstand higher temperatures but also to ensure environmental stability with a low recession rate [9], [10].

Another concern about EBCs is about both quasi-static and time-dependent mechanical properties, which are crucial to understand failure modes and develop reliable systems. Thermal cycling at high temperatures induces creep and sintering, thereby resulting in through-thickness cracking during cooling [11], [12], which may accelerate coating failure. It is therefore essential to know the thermomechanical behavior of EBCs. Among existing techniques, Zhu and Miller [13] have determined sintering and low-stress creep parameters using a dilatometer in isothermal conditions on self-supported ceramic coatings. The results appeared to be similar to those obtained with laser creep/sintering tests [12], where the system was uniformly heated on the coating surface, and high temperature mechanical tests [14], [15].

In all those cases, in order to identify and validate constitutive laws, comparisons between experiments and modeling are required, hence the development of various identification methods [16], some of them based on full-

field measurements [17]. Among these techniques, Finite Element Model Updating (FEMU) is widely used [18]–[21]. It is an iterative method based on the minimization of the norm of residuals between numerical and experimental data that can be displacement fields (FEMU-U), load levels (FEMU-F) or combinations of both (FEMU-UF) for instance [17]. Last, in addition to using measured displacement fields as raw data, some works [20]–[22] have proposed weighted FEMU based on the covariance matrix of measurement errors, which is considered in this study as well.

In the following, a high temperature test on an environmental barrier coated CMC is first presented. Full-field measurement techniques at high temperature are then introduced with infrared thermography and Digital Image Correlation (DIC). Last, the calibration of creep parameters is proposed using sequentially FEMU based on displacement *and* temperature fields.

2 Materials and experimental set-up

2.1 Tested materials

The tested sample is a ca. 3 mm thick CERASEP® A600 SiC/SiC composite made by SAFRAN Ceramics, whose length and width are respectively 95 and 20 mm. The substrate is then coated with a thin layer of (Si) bond coat, and finally with an EBC made of rare earth silicate. The length of the coated surface is 86 mm. The system is then heated in a furnace to stabilize the coating.

As mentioned before, the nonlinear behavior of the coating is essential to understand and quantify failure modes. In order to describe primary creep, a Norton-Bailey law is commonly used [11], [12], [14]

$$\dot{\tilde{\varepsilon}}^{cr} = Ar_0 \cdot e^{-\frac{E_a}{RT}} \cdot \tilde{\sigma}^n \cdot t^m \quad (1)$$

with

$$\dot{\tilde{\varepsilon}}^{cr} = \sqrt{\frac{2}{3}\dot{\boldsymbol{\varepsilon}}^{cr} : \dot{\boldsymbol{\varepsilon}}^{cr}} \quad (2)$$

where $\dot{\tilde{\varepsilon}}^{cr}$ is the equivalent creep strain rate, $\dot{\boldsymbol{\varepsilon}}^{cr}$ the creep strain tensor, Ar_0 the pre-exponential factor, E_a the creep activation energy, R the gas constant, T the absolute temperature, $\tilde{\sigma}$ the Von mises equivalent stress, n the creep stress exponent, t time and m the creep time exponent.

In the following, the initial value of the creep stress exponent n and time exponent m were taken from Ref. [23] for a similar material (i.e., $n = 0.9$ and $m = 0.78$). Over the investigated temperature range, the creep activation energy was provided by Safran and is equal to 272 ± 27 kJ/mol.

2.2 Experimental set-up and performed test

Figure 1 displays a high power (3kW) high heat flux CO_2 laser locally heating the sample described in Section 2.1. This thermal loading induces multiaxial (in-plane and through-thickness) thermal gradients. Under such conditions, the material expands and deflects. To measure the thermomechanical fields of the sample, the top surface is monitored using a middle-wave infrared (IR) camera (FLIR X6580sc) for temperature fields, a visible light camera (AVT Pike-421 with 4/80 lens and 41 mm extension ring) is positioned to measure the edge motion of the sample thanks to LED lighting (GS VITEC Multiled PT). The backside is monitored using bichromatic (IGAR6, Lumasens) and monochromatic (MI3, Raytek) pyrometers.

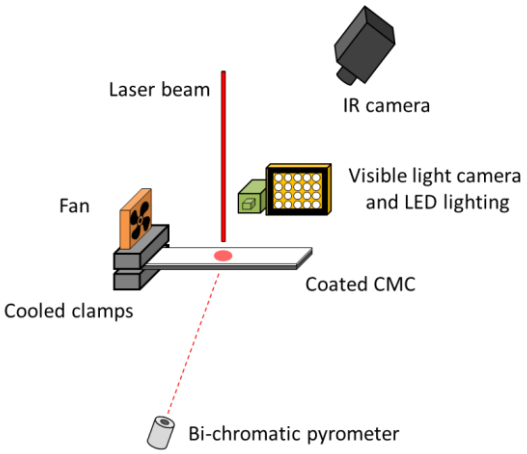

FIGURE 1: High temperature test monitored with infrared and visible light cameras

The test consists of three heating steps, each applied for 1 h. The maximum temperature is limited to 1350°C in order to avoid sintering of the coating, the latter would induce variations in Young's modulus [24]. During the test, thermal and visible light images were continuously acquired with a period of 2s. Figure 2 shows the laser power, dimensionless **front** and backside temperature profiles.

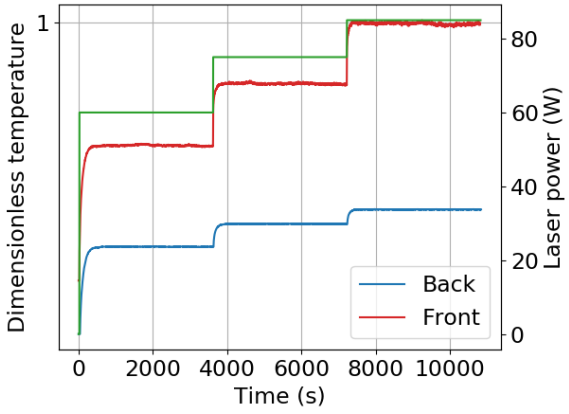

FIGURE 2: Laser power in green, dimensionless temperature profiles measured by the infrared camera in red and by the pyrometer in blue during the test

Hardware parameters of the optical and infrared systems are summarized in Table 1 and Table 2.

TABLE 1: DIC hardware parameters

Camera	AVT PIKE F-421 (monochrome detector)
Camera definition	2048 x 2048 pixels
Filter	Schneider Kreuznach Band pass Filter, BP 540-70 HT
Grey Levels amplitude	8 bits
Lens	Schneider Kreuznach 2.8/50
Field of view	see text
Image scale	see text
Image acquisition rate	0.5 fps
Exposure time	25 ms

TABLE 2: IR hardware parameters

Camera	FLIR X6580SC
Camera definition	640 x 512 pixels
Digital Levels amplitude	14 bits
Field of view	see text
Pixel size	200 µm
Image acquisition rate	0.5 fps
Integration time	30 µs

3 Full field measurements at high temperature

In this section, measurement of temperature and displacement fields are first detailed in a generic way, and then applied to the test described in the previous section.

3.1 Temperature field measurement

3.1.1 Calibration

Accurate temperature field measurement is essential not only to control the maximum temperature but also to estimate thermal gradients (*i.e.* the stress level). In quantitative monochromatic thermography, the knowledge of the emissivity is required to assess the true temperature

$$L_\lambda(T) = L_\lambda^0(T_R) = \varepsilon_\lambda(T)\, L_\lambda^0(T) \tag{3}$$

where L_λ is the spectral radiance, T the true absolute temperature, L_λ^0 the blackbody spectral radiance, T_R the radiance or blackbody temperature, and ε_λ the spectral emissivity. As the device used to measure temperature fields is a middle wavelength infrared camera [3 µm ; 5 µm] with a band-pass filter at 4 µm, the emissivity has been measured by CEMHTI (Orléans, France) [25], [26] and is shown in Figure 3, at this wavelength, from a few hundred degrees Celsius to the same maximum temperature as in Figure 2. The measured total emissivity is also plotted and will be used in Section 4.1.1.

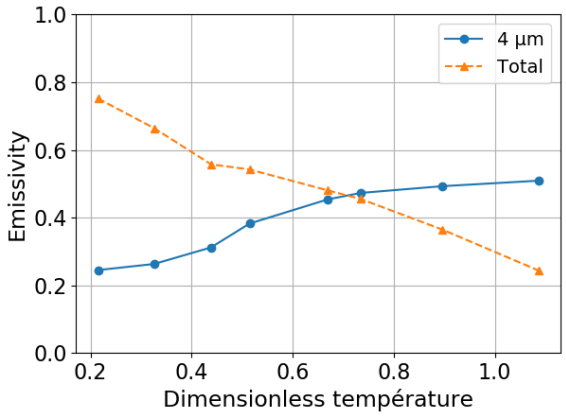

Figure 3: Spectral emissivity at 4 µm and total emissivity measured on the environmental barrier coating

The sensor is sensitive to the radiant flux coming from the thermal scene, which is converted into digital levels (DL) and then translated into temperature with the emissivity of the observed surface. Digital levels are expressed with a calibration law [27] as

$$U = s\,[\varphi_o(T) + \varphi_e(T) + k(T_{cam}^4 - T_d^4)\,]\,IT + U_0 \tag{4}$$

where U is the measured tension, s the sensitivity of the sensor, $\varphi_o(T)$ the radiant flux coming from the object, $\varphi_e(T)$ the radiant flux coming from the environment, $k(T_{cam}^4 - T_d^4)$ the radiant flux coming from the camera housing, IT the integration time, and U_0 a digital offset.

The global radiant flux is expressed in Equation (4) as the sum of three contributions. In this case, given the range of temperature, the radiant flux from the object is prevalent. In addition, because of the band-pass filter, the camera is monochromatic and the radiant flux from the object can be directly related with Planck's law for a blackbody. These assumptions lead to some simplifications of Equation (4)

$$U = p \cdot \left[\frac{C_1 \lambda^{-5}}{e^{\left(\frac{C_2}{\lambda T}\right)} - 1}\right] \cdot IT + U_0 \tag{5}$$

with p and U_0 constants to identify, C_1 and C_2 parameters of Planck's equation. This calibration expression is then identified with the manufacturer data on a blackbody for several integration times as shown in Figure 4. The good agreement enables for the use of Equation (5) on the real material.

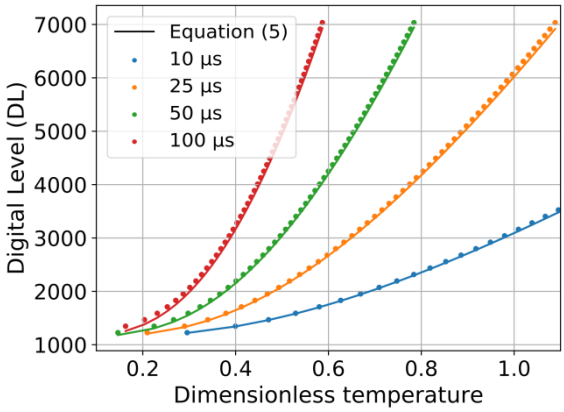

FIGURE 4: Calibration data by FLIR® **manufacturer** and estimation for several integration times

Last, for a tested sample the emissivity of which is known in the same conditions, depending on the temperature and at the wavelength of the band-pass filter, Equation (5) becomes

$$U = p * \left[\epsilon(T,\lambda) * \frac{C_1 \lambda^{-5}}{e^{\left(\frac{C_2}{\lambda T}\right)} - 1} \right] * IT + U_0 \qquad (6)$$

To check all these assumptions, residuals between a temperature field rebuilt using Equation (6) and the built-in calibration data for an emissivity of 0.5, and an integration time of 25 µs are shown in Figure 5(b) for a heating with high thermal gradients (Figure 5(a)). heterogeneous residuals are observed with maximum values at both highest and lowest DLs, which is explained for low temperatures by getting close to the lower bound of the calibration range.

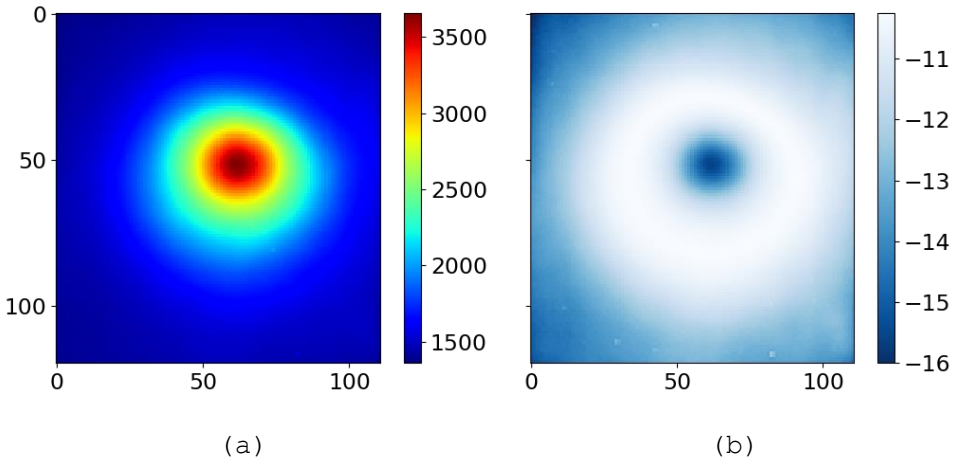

FIGURE 5: (a) DL field measured on the studied EBC, and (b) residuals (°C) between Equation (6) and the manufacturer calibration data

3.1.2 Application to the test

Figure 6 shows the three average temperature fields during the steady state heating steps. This range of temperatures is included in the calibration range described in the previous section. It is also worth noting that the laser beam is smaller than the width of the sample, thereby generating high surface thermal gradients and thermomechanical stresses different from isothermal conditions.

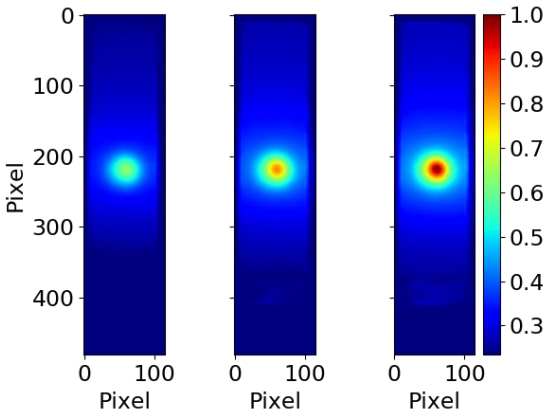

FIGURE 6: Average dimensionless temperature fields at the three stabilized heating steps

3.2 Digital image correlation at high temperatures

DIC was used numerous times as a non-contacting full-field measurement technique [17] at room temperature [28]. It has been proven to be efficient in high temperature tests since the pioneering work of Lyons *et al.* [29] where the authors tested samples up to 650°C. Tests were then performed at higher temperatures with DIC. Pan *et al.* [30], Grant *et al.* [30] reached temperatures as high as 1200°C, Leplay *et al.* reached 1350°C [32], Novak and Zok [33] 1500°C. These works highlighted some challenges:

- Gray level conservation may be violated. To circumvent this issue, filtering thermal radiations via lighting with band-pass filters is one possible experimental solution [30], [31], [33]. Brighness and contrast corrections during the DIC procedure is another route, be it for local DIC [28] or global approaches [34]–[36].
- Fluctuations due to heat haze effects impact the measurement by creating artifacts of the optical path. Using forced air flux [29], [33], or spatiotemporal DIC [37], [38] are two possible solutions to mitigate these effects.

- For stability, high temperature speckles are required. Various coatings made of nitride and aluminum oxides [29], or cobalt oxide mixed with inorganic adhesive [30] have been used. High temperature powders are another potentially durable solution [39], [40].

3.2.1 Global DIC framework

Global DIC considers the minimization of the gray level residuals over the whole region of interest (ROI). It ensures continuity of the displacement fields, which is assumed to be true in this work. The gray level conservation at any pixel location reads

$$g\big(\boldsymbol{x}+\boldsymbol{u}(\boldsymbol{x})\big)=f(\boldsymbol{x}) \tag{7}$$

where f is the gray level image in the reference configuration, g in the deformed configuration, $\boldsymbol{x}$ any pixel in the ROI, $\boldsymbol{u}(\boldsymbol{x})$ the sought displacement field. The correlation procedure aims to find $\boldsymbol{u}$ that minimize the L2-norm of the gray level residual η defined as

$$\eta(\boldsymbol{x})=f(\boldsymbol{x})-g\big(\boldsymbol{x}+\boldsymbol{u}(\boldsymbol{x})\big) \tag{8}$$

As the minimization of the squared norm of η over the whole region of interest Ω is an ill-posed problem, the displacement field is decomposed as

$$\boldsymbol{u}(\boldsymbol{x})=\sum_{i} u_i\,\boldsymbol{\theta}_i(\boldsymbol{x}) \tag{9}$$

where $\boldsymbol{\theta}_i$ are chosen shape functions and u_i the associated nodal displacements to determine. The Gauss-Newton iterative procedure [21] that solves linear systems written in terms of displacement corrections $\{\delta\boldsymbol{u}\}$ reads

$$[\boldsymbol{M_{DIC}}]\{\boldsymbol{\delta u}\} = \{\boldsymbol{b}\} \quad (10)$$

where $[\boldsymbol{M_{DIC}}]$ is the Hessian matrix, $\{\boldsymbol{\delta u}\}$ the vector gathering all the amplitude corrections and $\{\boldsymbol{b}\}$ the residual column vector. In this work, mechanical regularization [41] is also used to enforce mechanical admissibility to the displacement fields. Table 3 summarizes the DIC parameters used hereafter.

TABLE 3: DIC analysed parameters

DIC software	Correli 3.0 [42]
Image filtering	none
Element length	20 px
Regularization length	200 px
Shape functions	linear (T3)
Mesh	regular
Interpolant	cubic
Displacement noise-floor	0.02 px

3.2.2 Application to the test

Figure 7 shows the reference image of the monitored edge of the sample during the test. To get a homogeneous background, a high temperature black paint (AREMCO® 840-M) was applied first, followed by a boron nitride white paint to obtain a random pattern. During the test, the left part of the sample was held in grips.

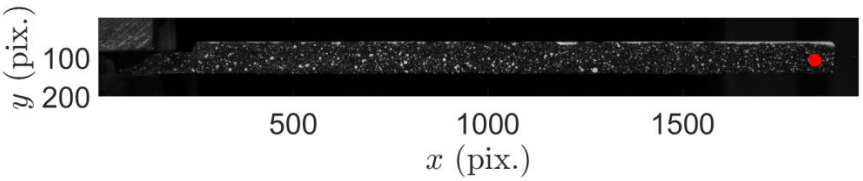

Figure 7: Reference image of the coated CMC with its speckle pattern. The red dot on the right side of the sample corresponds to the location of the point for which temporal profiles are plotted hereafter.

The displacement fields are shown in Figure 8 after 200s of heating. First, the benefit of mechanical regularization [41] is visible and suitable with continuous displacement fields in both directions, which is assumed to be true in this case. It is also worth noting that the magnitude of the displacements, particularly in the Y direction, does not exceed 0.5 px (or 28 µm).

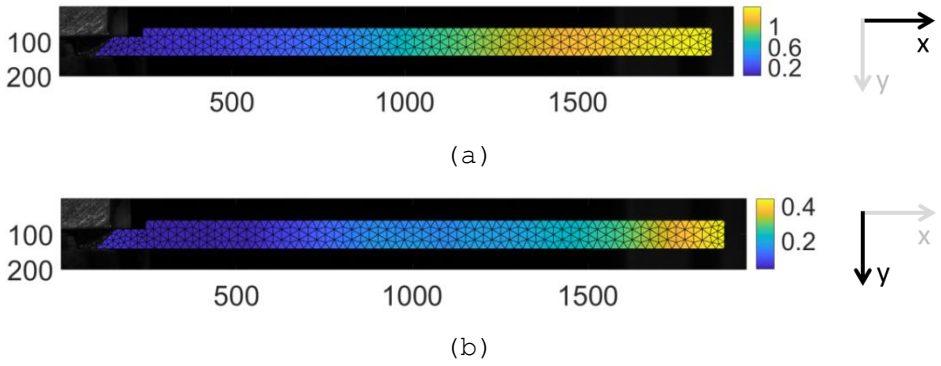

Figure 8: Displacement fields at $t = 200\,s$ in (a) the X and (b) Y-directions expressed in pixel (1 pixel is equal to 55 µm)

Given the range of temperatures reached on the edge of the sample, LED lighting and an optical filter are enough to avoid large gray level changes due to high temperatures [29], [33]. This assumption is confirmed in Figure 9 in which the gray level residuals are plotted between the first image and an image in the middle of the last step. It is observed that the mean residual on the black coated surfaces

is close to 0 (Root Mean Square residual is equal to 6 GL) whereas dots appear where there are white speckles. This is due to a darkening of the boron nitride coating, which is visible after the test.

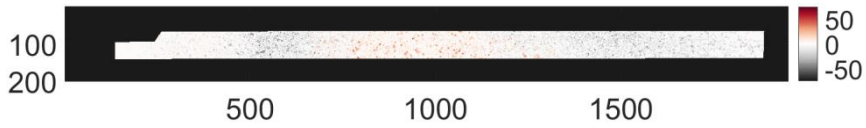

Figure 9: Gray level residuals (GL) between the first image and an image in the middle of the last step

In Figure 10, displacements are plotted for the red dot shown in Figure 7 at the end of the sample. Rigid body motions of the grips have been removed to obtain relative displacements and plot a deflection. The elongation curve clearly shows the three heating levels. There is no large variation between each step (*i.e.* from ~1.5 to ~2 px) as only a small part of the EBC is heated in this test (Figure 6). The deflection profile shows nonlinearities at the beginning of each step. More explanations are given hereafter.

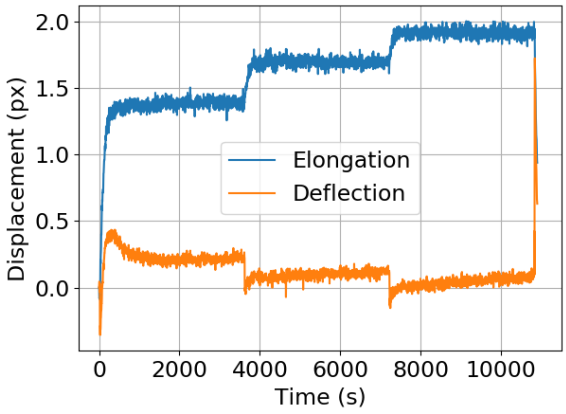

Figure 10: Displacements of the red dot (Figure 7) during the test (1 pixel is equal to 55 µm)

The next section will introduce the FE model used with various hypotheses on the coating behavior, and first

comparisons between measured and computed displacements are carried out.

4 Identification strategy

4.1 Thermomechanical modeling

This part describes the finite element model (FEM) used herein to describe the test and the choices and hypotheses made to estimate thermomechanical parameters.

4.1.1 Thermal model

The tested sample is modeled as an assembly of two parts, one representing the SiC/SiC composite and one the EBC (Figure 11). Neither the Si bond coat layer nor the grips are accounted for. In the following analysis, the thermomechanical parameters of the CMC part are assumed to be known and will not be calibrated.

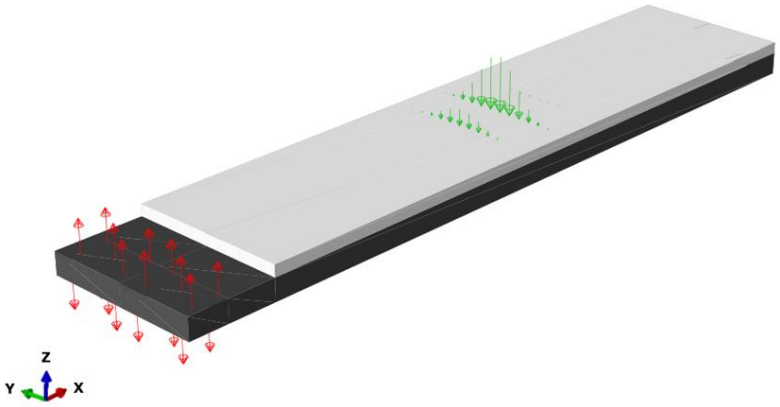

FIGURE 11: Thermomechanical model with thermal loads (green arrows) from the laser heating and heat loss in the grips (red arrows)

Let us consider the first heating level (both transient and steady states) of the experiment presented in Section 2.1. The thermal load induced by the laser beam is parameterized as a heat flux applied to the top surface of

the sample (downward green arrows on the EBC surface in Figure 11). This flux ϕ is assumed to be super Gaussian and is modeled with six parameters

$$\phi = A\, e^{-\left[\left(\frac{x-X_c}{B_x}\right)^k + \left(\frac{y-Y_c}{B_y}\right)^k\right]} \tag{11}$$

where A denotes the laser power, B_x and B_y the widths of the laser beam (respectively, along the x-axis and y-axis), k the power of the super Gaussian, X_c and Y_c the center coordinates of the laser beam.

The effect of the grips is modeled as heat losses on the top and bottom areas of the CMC material (depicted by red arrows in Figure 11), with a constant amplitude ϕ_0.

Thermal exchanges are also considered in the heat transfer model. Given the high temperatures, radiation exchanges are prevalent. The total emissivity measured on the EBC and plotted in Figure 3, is used for the top white surface. For all the other surfaces, since they are coated with black paint, the total emissivity provided by the manufacturer is considered. Last, convection is also accounted for with an exchange coefficient depending on the temperature and whether it is the top or bottom surface **[43]**.

4.1.2 Thermomechanical model

The initial hypothesis made on the coating behavior is thermoelasticity, with temperature-dependent thermomechanical parameters. A qualitative comparison is made between measured displacements (elongation and deflection profiles) and computed displacements (Figure 12) for the first heating step. For all further analyses, the computed displacements (in metric units) are expressed in DIC units (i.e., pixels).

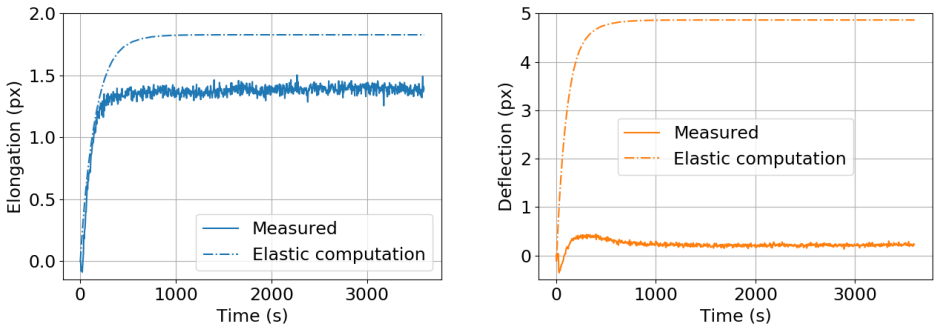

(a) (b)

FIGURE 12: (a) Elongation (in blue) and (b) deflection (in orange) at the end of the sample obtained by DIC (solid line) and thermoelastic computation (dashed line), 1 pixel is equal to 55 µm

Two conclusions can be drawn from Figure 12. First, the difference of amplitudes between measured and computed displacements highlights the need for adjusting the thermomechanical parameters by updating the FE model. Second, as seen on the deflection results and expected from the results of Section 2.1, the nonlinear response of the sample (measured by DIC) cannot be described by thermoelasticity. Therefore, creep parameters, taken from Ref. [23] and the EBC maker, are added to the model. Figure 13 compares the measured elongation (in blue) and deflection profiles (in orange) and the computed quantities with the creep parameters introduced previously.

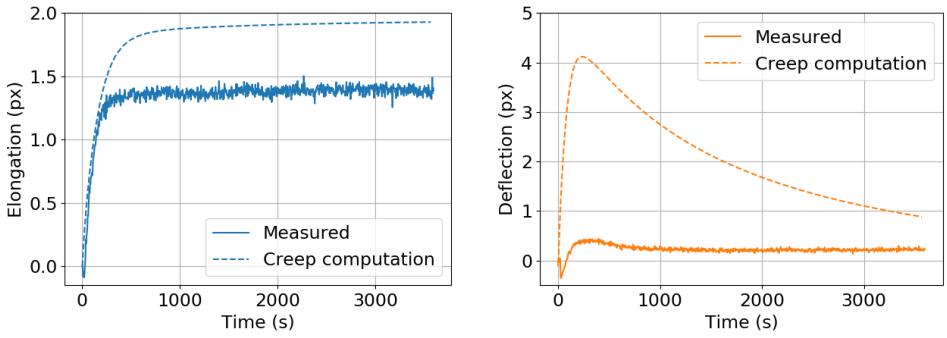

(a) (b)

FIGURE 13: (a) Elongation (in blue) and (b) deflection (in orange) at the end of the sample obtained by DIC (solid line) and computed (dashed line). The FE computation uses the creep law identified using TMA tests.

Measured and computed displacements are now qualitatively comparable. The nonlinear behavior of the coating expresses itself on the deflection profile for about 200 s, which is due to to the activation of coating creep. Further, in the computation (between 1,500 s and 3,600 s), creep brings the sample to an equilibrium position as observed on the measurements. However, the computed values are far from the measured ones, especially creep activation that is faster experimentally. These variations are mainly due to differences in composition of the processed air plasma sprayed EBC but also in the deposition parameters. Besides, it may also be due to (1) an asymmetric creep behavior between tension and compression of the coating, which has already been observed in ceramics [32], [44], [45], (2) change of creep parameters for higher stress levels as the maximum loading of TMA tests is 40 MPa whereas the compressive stresses reached by the reported test are greater than 150 MPa. Thus, the creep stress and time exponents and the thermomechanical parameters will be updated in the following section.

To complete the thermomechanical model of the experiment, the mechanical boundary conditions are assessed. In the best

case, mechanical boundary conditions would correspond to clamping in the grips. However, the analysis of displacements close to the grips (left part of the green mesh in Figure 14) shows significant motions, compared to those plotted in Figure 10 in both directions. For this reason, boundary conditions applied to the FE model are those measured, spatially interpolated on the FE mesh and applied to the left vertical line on the red mesh shown in Figure 14.

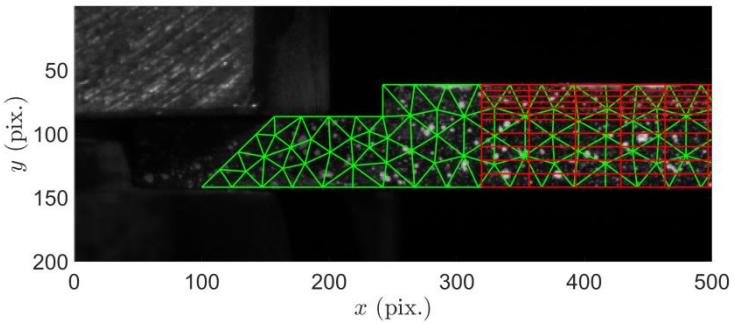

FIGURE 14: Focus on the area close to the grips with both DIC (in green) and FE (in red) meshes

The next section will introduce the identification procedure chosen to assess the parameters of the described thermomechanical model.

4.2 Identification procedure

In this section, notations $[\underline{\boldsymbol{X}}]$ and $\{\underline{\boldsymbol{X}}\}$ refer to spatiotemporal matrix or vector.

4.2.1 Finite Element Model Updating

The *FEMU-TU* identification procedure [18], [19] aims to calibrate the sought parameters $\{\boldsymbol{p}\}$ of an FE model by minimizing the global functional χ^2_{TU} on thermal (T) and displacement (U) fields

$$\chi^2_{TU}(\{\boldsymbol{p}\}) = \omega\,\chi^2_T(\{\boldsymbol{p}\}) + (1-\omega)\chi^2_U(\{\boldsymbol{p}\}) \tag{12}$$

where χ_T is the thermal cost function, χ_U the kinematic cost function, and ω the weighting factor between thermal and kinematic contributions.

The *FEMU-TU* procedure relies on a simultaneously weighted [20]-[22] least squares minimization of thermal and displacement residuals. The residuals for a field X (where X denotes the temperatures T or nodal displacements $\boldsymbol{U}$) is defined as the difference between the measured data $\{\underline{\boldsymbol{X}}_{\boldsymbol{m}}\}$ and the computed ones $\{\underline{\boldsymbol{X}}_{\boldsymbol{c}}(\{\boldsymbol{p}\})\}$, where the latter ones are projected in space on the measurement mesh and in time on the experimental time basis. The weighting of each cost function is made by considering the number of data acquired and used for the minimization (in space N_X and in time $N_{t,X}$), and by the associated uncertainties on measurements of the field X (through the covariance matrix $[\underline{\boldsymbol{C}}_{\boldsymbol{X}}]$ discussed in the following section). Therefore, the thermal and kinematic cost functions are written as

$$\chi^2_T(\{\boldsymbol{p}\}) = \frac{1}{N_T N_{t,T}}\left(\{\underline{\boldsymbol{T}}_{\boldsymbol{m}}\} - \{\underline{\boldsymbol{T}}_{\boldsymbol{c}}(\{\boldsymbol{p}\})\}\right)^t [\underline{\boldsymbol{C}}_{\boldsymbol{T}}]^{-1}\left(\{\underline{\boldsymbol{T}}_{\boldsymbol{m}}\} - \{\underline{\boldsymbol{T}}_{\boldsymbol{c}}(\{\boldsymbol{p}\})\}\right) \tag{13}$$

and

$$\chi^2_U(\{\boldsymbol{p}\}) = \frac{1}{N_U N_{t,U}}\left(\{\underline{\boldsymbol{U}}_{\boldsymbol{m}}\} - \{\underline{\boldsymbol{U}}_{\boldsymbol{c}}(\{\boldsymbol{p}\})\}\right)^t [\underline{\boldsymbol{C}}_{\boldsymbol{U}}]^{-1}\left(\{\underline{\boldsymbol{U}}_{\boldsymbol{m}}\} - \{\underline{\boldsymbol{U}}_{\boldsymbol{c}}(\{\boldsymbol{p}\})\}\right) \tag{14}$$

The *FEMU-TU* algorithm iteratively updates the parameters by minimizing thermal and kinematic spatiotemporal residuals (gathered in the weighted right-handside vectors $\{\underline{\boldsymbol{B}}_{\boldsymbol{X}}\}$)

$$\{\boldsymbol{\delta p}\} = \left(\omega[\underline{\boldsymbol{H}}_{\boldsymbol{T}}] + (1-\omega)[\underline{\boldsymbol{H}}_{\boldsymbol{U}}]\right)^{-1}\left(\omega\{\underline{\boldsymbol{B}}_{\boldsymbol{T}}\} + (1-\omega)\{\underline{\boldsymbol{B}}_{\boldsymbol{U}}\}\right) \tag{15}$$

The search direction is given by the global Hessian matrix $[\underline{\boldsymbol{H}}]$, defined as the weighted sum of thermal and kinematic Hessians

$$[\underline{\boldsymbol{H}}] = \omega[\underline{\boldsymbol{H}}_{\boldsymbol{T}}] + (1-\omega)[\underline{\boldsymbol{H}}_{\boldsymbol{U}}] \tag{16}$$

In a Bayesian approach, the weighting factor between the thermal and kinematic parts (introduced in Equation (12)) reads [46]

$$\omega = \frac{N_T N_{t,T}}{N_T N_{t,T} + N_U N_{t,U}} \tag{17}$$

A relevant way to assess the sensitivity of the sought parameters is to analyze the Hessian matrices [47]. The Hessian matrix of a field X depends on the sensitivity matrix $[\underline{\boldsymbol{S}}_{\boldsymbol{X}}]$ (gathering the sensitivity vectors $\{\underline{\boldsymbol{S}}_{\boldsymbol{X},\boldsymbol{p_i}}\}$ of the measured data with respect to an independent variation of each parameter p_i)

$$[\underline{\boldsymbol{H}}_X] = \frac{[\underline{\boldsymbol{S}}_X]^t [\underline{\boldsymbol{C}}_X]^{-1} [\underline{\boldsymbol{S}}_X]}{N_X N_{t,X}} \tag{18}$$

with

$$\{\underline{\boldsymbol{S}}_{\boldsymbol{X},\boldsymbol{p_i}}\} = \frac{\{\underline{\boldsymbol{X}}_{\boldsymbol{c}}(\{\boldsymbol{p}_{\boldsymbol{dist,i}}\})\} - \{\underline{\boldsymbol{X}}_{\boldsymbol{c}}(\{\boldsymbol{p}_{\boldsymbol{ref}}\})\}}{\varepsilon} \tag{19}$$

The set of reference parameters is denoted $\{\boldsymbol{p}_{\boldsymbol{ref}}\}$ and the set of perturbed parameters used to compute $\{\boldsymbol{S}_{\boldsymbol{X},\boldsymbol{p_i}}\}$ is denoted $\{\boldsymbol{p}_{\boldsymbol{dist,i}}\}$ and is equal to the reference set with the i^{th} parameter p_i varied with an offset ε (taken here equal to 5% of reference value for all parameters, except for those corresponding to a position where the perturbation is made

proportionally to the length of the coating). Thus, the sensitivity analysis consists in computing the solution with the initial set of parameters (reference thermal and kinematic fields) then comparing it with solutions from computations with perturbed parameters.

In the following section, the results of such analysis are presented to assess which parameters of the previously described model (Section 4.1) can be calibrated with regards to uncertainties on thermal and kinematic measurements, and the corresponding identification strategy.

4.2.2 Sensitivity analysis

The following sensitivity analysis is performed by computing only one level of heating close to the first heating step, with both transient and steady states. For the sensitivity analysis, the selected thermal parameters $\{\boldsymbol{p_{th}}\}$ are the six parameters describing the thermal load ϕ (A, B_x, B_y, k, X_c, Y_c), and the amplitude of bottom surface heat losses ϕ_0. Regarding the thermomechanical parameters $\{\boldsymbol{p_{thm}}\}$, two material properties are analysed, namely the in-plane thermal expansion α_x (equal to α_y) and creep. The first one is parameterized as a first order transformation of the initial law (i.e., $\alpha_{x,update} = \alpha_{x,init}\,(a\,T + b)$). The second one is described by the two powers n and m, leading to a total of 12 parameters for the sensitivity analysis.

In the sequel, the effect of the weighting factor ω between thermal and kinematic data is analyzed. The results are compared to a Bayesian approach, with a value of ω expressed by Equation (17) (and here equal to 0.73, i.e. the global functional is mostly dependent on thermal data), and for different arbitrary values of ω, prescribed by the user. In the last case, the value of ω ranges from 0 (pure *FEMU-U* analysis) to 1 (pure *FEMU-T* analysis).

The different global Hessian matrices are reported in Figure 15. The Hessian is represented as a square matrix of size the number of parameters, where the values of the absolute components are expressed in logarithmic scale (base 10) and where the sign of the components (plus or minus) of the matrix is plotted for each component. Thus, a high value of the component of the diagonal of the Hessian matrix corresponds to a high sensitivity of such parameter. Couplings between parameters are quantified by the off-diagonal components and can also be assessed with the eigenvectors of the diagonalized Hessian matrix.

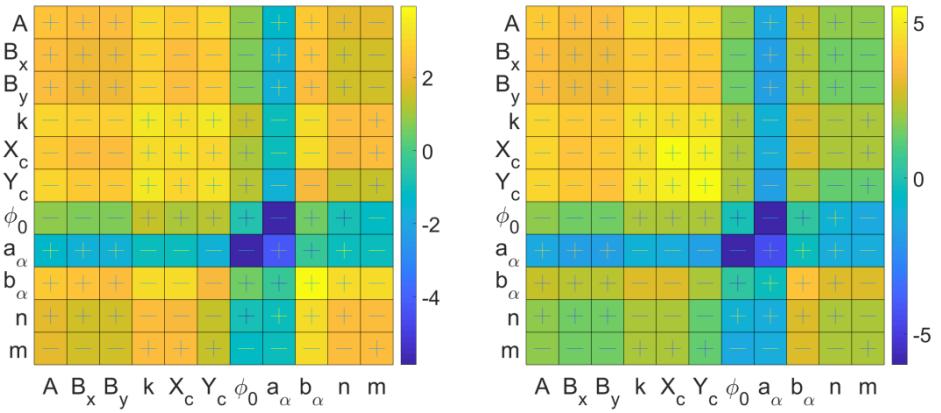

(a) $\omega = 0$ (b) $\omega = 0.25$

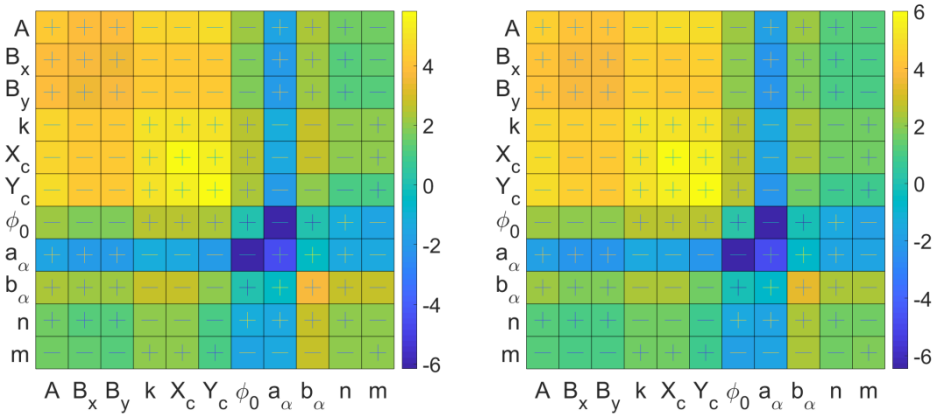

(c) $\omega = 0.5$ (d) $\omega = 0.75$

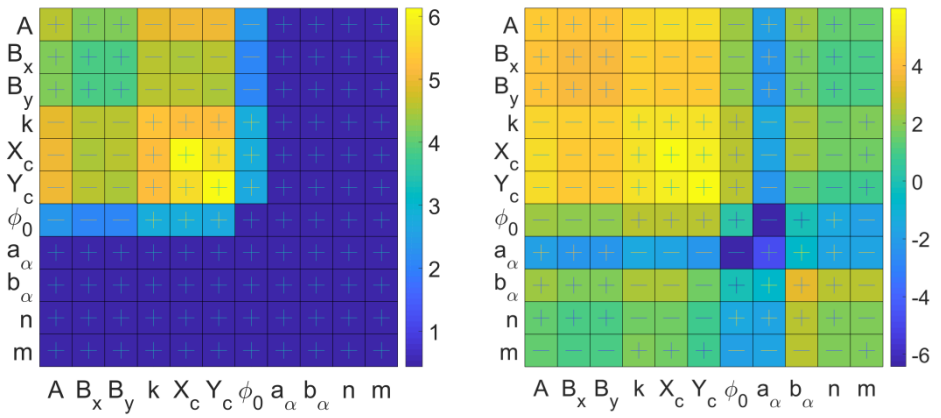

(e) $\omega = 1$ (f) Bayesian weighting

Figure 15: Global Hessian matrix in log-10 scale with different weighting factors ω

First, it can be noticed that for all values of the weighting factor ω, the term H_{77} is very small, which means that the heat loss parameter ϕ_0 cannot be calibrated. Conversely, its effect is completely negligible in comparison with all the other parameters. Therefore, it will not be considered in the final identification procedure.

Second, a Bayesian approach for the *FEMU-TU* functional (i.e $\omega = 0.73$) leads to a high sensitivity of the thermal parameters and makes the identification of the thermomechanical properties of the coating more difficult. The analysis of the eigenvalues and eigenvectors of the Bayesian Hessian matrix (Figure 16) highlights its bad conditioning. It can be seen that there are 3 to 4 orders of magnitude between the first eigenvalues (whose associated eigenvectors are driven by thermal loading parameters) and the eigenvalues associated with creep and thermal expansion contributions.

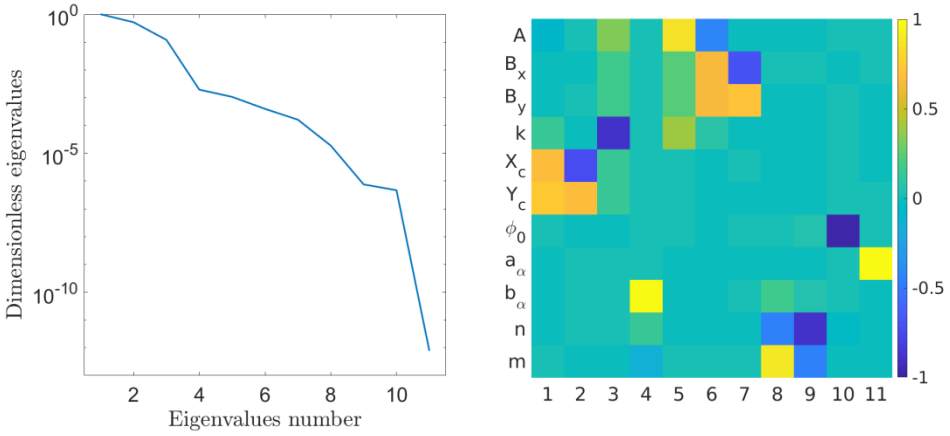

(a) (b)

FIGURE 16: Dimensionless (a) eigenvalues and (b) eigenvectors of the global Bayesian Hessian matrix ($\omega = 0.73$)

The analysis of Hessian matrices is conducted with prescribed weighting factors (especially $\omega < 0.73$) to improve the sensitivity to thermomechanical parameters. Figure 17

and Figure 18 (representing the eigenvalues and eigenvectors of the Hessian matrix) show that even for a small value of ω (e.g., 0.25), the contribution of thermal parameters reduces considerably the sensitivity of the thermomechanical properties, with a ratio of 2 to 3 orders between the first eigenvalue and the fourth one.

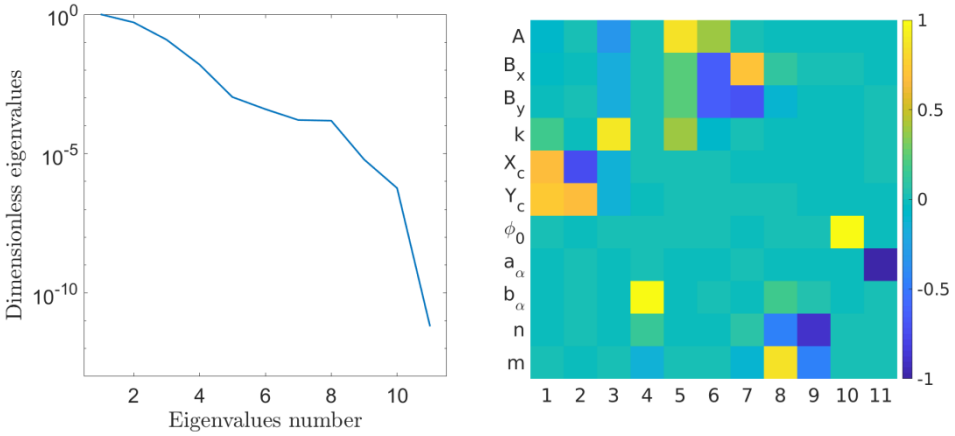

(a) (b)

FIGURE 17: Dimensionless (a) eigenvalues and (b) eigenvectors of the global Hessian matrix computed with $\omega = 0.25$

Thus, to avoid this effect, the weighting factor should be set to 0, i.e. using only kinematic data to calibrate both thermal and thermomechanical properties at once. In that case, the Hessian matrix shows that all parameters have similar sensitivities, with a high level with respect to acquisition noise on DIC measurements. The eigenvector associated with the first eigenvalue of the Hessian matrix (Figure 18) highlights the contribution of the parameters describing thermal expansion and creep, along with three out of six parameters of thermal loading.

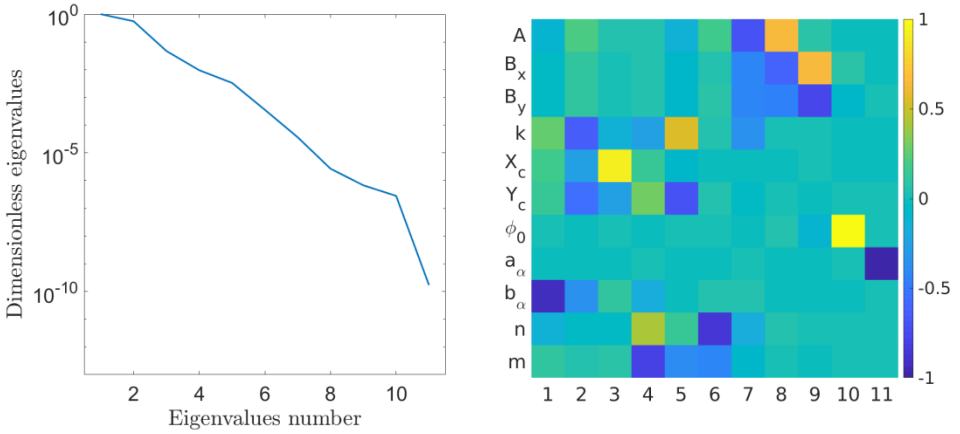

(a) (b)

FIGURE 18: Dimensionless (a) eigenvalues and (b) eigenvectors of global Hessian matrix computed with $\omega = 0$

However, performing a single identification through *FEMU-U* does not appear as a good choice since it will exclude from the analysis 73% of the total amount of data of the experiment (thermal data), leading to higher uncertainties on thermal loading (parameters A, B_x and B_y).

Therefore, it is concluded from this sensitivity analysis that a good identification strategy is to perform two uncoupled *FEMU* steps. It is beneficial to run first a *FEMU-T* analysis to calibrate the six thermal parameters (A, B_x, B_y, k, X_c, Y_c), using only IR camera data, then to perform a *FEMU-U* calibration of the five thermomechanical parameters describing creep and thermal expansion.

4.2.3 Implemented schemes

As concluded for the previous section, the calibration strategy is a two-step uncoupled *FEMU-T/FEMU-U* procedure. The algorithm first runs and calibrates the thermal loading parameters $\{\boldsymbol{p_{th}}\} = \{A, B_x, B_y, k, X_c, Y_c\}^t$, for each temperature level, independently, by minimizing the residuals between measured and computed temperatures. Thus, from one step to another, besides its amplitude, the shape of the super-Gaussian

(position of laser center, width, and shape) may evolve. For each step, only the steady state part is considered to get a first (and fast) estimate of the loading parameters. The algorithm iteratively updates the thermal parameters $\{\boldsymbol{p_{th}}\}$ (according to functional $\chi_T^2(\{\boldsymbol{p_{th}}\})$ by determining the new correction vector $\{\boldsymbol{\delta p_{th}}\}$

$$\{\boldsymbol{\delta p_{th}}\} = \left[\underline{\boldsymbol{H}}_{\boldsymbol{T}}\right]^{-1}\{\underline{\boldsymbol{B}}_{\boldsymbol{T}}\} \tag{20}$$

with $\left[\underline{\boldsymbol{H}}_{\boldsymbol{T}}\right]$ defined in Equation (18) and

$$\{\underline{\boldsymbol{B}}_{\boldsymbol{T}}\} = \frac{1}{N_T N_{t,T}}\left[\underline{\boldsymbol{S}}_T\right]^t\left[\underline{\boldsymbol{C}}_T\right]^{-1}\left(\{\underline{\boldsymbol{T}}_{\boldsymbol{m}}\} - \{\underline{\boldsymbol{T}}_{\boldsymbol{c}}(\{\boldsymbol{p_{th}}\})\}\right) \tag{21}$$

where $\left[\underline{\boldsymbol{C}}_T\right]$ is a diagonal matrix with a variance depending on the temperature level to weight temperatures according to their uncertainties. The values of the standard deviation were identified in other tests. The minimization stops once the magnitude of the new correction $\{\boldsymbol{\delta p_{th}}\}$ is less than 1%.

Once the thermal loading parameters are calibrated for the three temperature levels, the entire experiment is considered, with transient and steady states, for the FEMU-U identification. Thermal boundary conditions are set and the FEMU-U procedure runs, according to Equation (14), to calibrate the thermomechanical parameters $\{\boldsymbol{p_{thm}}\} = \{\alpha_x^1, \alpha_x^2, \alpha_x^3, n, m\}^t$ by iteratively computing the corrections $\{\boldsymbol{\delta p_{thm}}\}$

$$\{\boldsymbol{\delta p_{thm}}\} = \left[\underline{\boldsymbol{H}}_{\boldsymbol{U}}\right]^{-1}\{\underline{\boldsymbol{B}}_{\boldsymbol{U}}\} \tag{22}$$

with $\left[\underline{\boldsymbol{H}}_{\boldsymbol{U}}\right]$ defined in Equation (18) and, considering that $\left[\underline{\boldsymbol{C}}_{\boldsymbol{U}}\right] = 2\sigma_f^2\left[\underline{\boldsymbol{M}}_{DIC}\right]^{-1}$ [48], [49]

$$\{\underline{\boldsymbol{B}}_{\boldsymbol{U}}\} = \frac{1}{2\sigma_f^2 N_U N_{t,U}} [\underline{\boldsymbol{S}}_U]^t [\underline{\boldsymbol{M}}_{DIC}] (\{\underline{\boldsymbol{U}}_{\boldsymbol{m}}\} - \{\underline{\boldsymbol{U}}_{\boldsymbol{c}}(\{\boldsymbol{p}_{\boldsymbol{thm}}\})\}) \quad (23)$$

where $[\underline{\boldsymbol{M}}_{DIC}]$ is a block diagonal matrix constructed with the DIC Hessian matrix $[\boldsymbol{M}_{DIC}]$ introduced in Section 3.2.1, and σ_f the standard deviation of acquisition noise.

Moreover, to help convergence of each algorithm, an additional Tikhonov regularization is introduced [22], with

$$[\underline{\boldsymbol{H}}_{\boldsymbol{Tikh,X}}] = \lambda_{Tikh,X} [\underline{\boldsymbol{I}}] \quad (24)$$

and

$$\{\underline{\boldsymbol{B}}_{\boldsymbol{Tikh,X}}\} = \lambda_{Tikh,X} (\{\boldsymbol{p^0}\} - \{\boldsymbol{p}\}) ./ \{\boldsymbol{p^0}\} \quad (25)$$

where $[\underline{\boldsymbol{I}}]$ is the identity matrix, $\{\boldsymbol{p}\}$ the set of current parameters (i.e. $\{\boldsymbol{p}_{\boldsymbol{th}}\}$ or $\{\boldsymbol{p}_{\boldsymbol{thm}}\}$ depending on the *FEMU-X* procedure), $\{\boldsymbol{p^0}\}$ the initialization of $\{\boldsymbol{p}\}$ and $\lambda_{Tikh,X}$ the Tikhonov factor, computed here with respect to the largest eigenvalue $\lambda_{max,X}$ of the Hessian matrix $[\underline{\boldsymbol{H}}_X]$ (i.e. $\lambda_{Tikh,X} = \lambda_{max,X}\, 10^{itik}$). This regularization leads to a slight modification of each *FEMU-X* system

$$\{\boldsymbol{\delta p}\} = \left([\underline{\boldsymbol{H}}_X] + [\underline{\boldsymbol{H}}_{\boldsymbol{Tikh,X}}]\right)^{-1} \left(\{\underline{\boldsymbol{B}}_X\} + \{\underline{\boldsymbol{B}}_{\boldsymbol{Tikh,X}}\}\right) \quad (26)$$

The Tikhonov regularization is relaxed step by step, by reducing the value of $itik$ (i.e., decreasing $\lambda_{Tikh,X}$) until it possibly reaches the lower eigenvalues of the Hessian matrix $[\underline{\boldsymbol{H}}_X]$.

The following section presents the results obtained with the proposed identification strategy.

5 Discussion of the results

5.1 Thermal identification

The results are first presented and detailed for the first heating level. As mentioned in Section 4.1.1, the parameters to be determined are the laser loading, meaning that only results on the stabilized heating steps are analyzed. Figure 19 shows the Root Mean Square (RMS) residual during the minimization procedure. The RMS residual decreases from 66°C to 20°C, thereby showing the efficiency of the procedure (i.e a three-fold reduction). It is also worth noting that for the first two Tikhonov relaxations, the residuals decrease immediately and are stable. This is not the case for the third one.

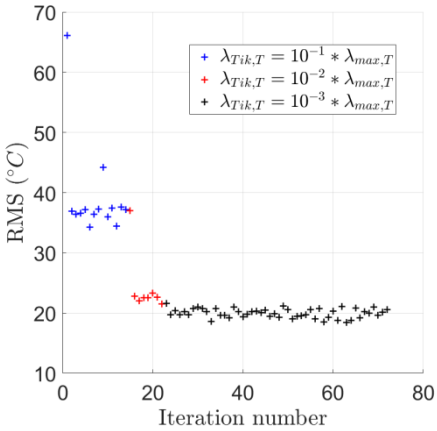

Figure 19: Root mean square residual (°C) history over the entire sample for the first heating step

Figure 20 shows the change of parameters during the procedure. As seen in Figure 15(e), the position of the center of the laser beam is the most sensitive parameter meaning that it is calibrated during the first Tikhonov relaxation (Figure 20(a)). In this case, it is even stable after one iteration. On the other hand, the amplitude of the laser beam, which is less sensitive, changes after the first Tikhonov relaxation. Oscillations during the third

relaxation are due to the coupling of the amplitude with the width of the laser as indicated on the Hessian matrix in Figure 15(e).

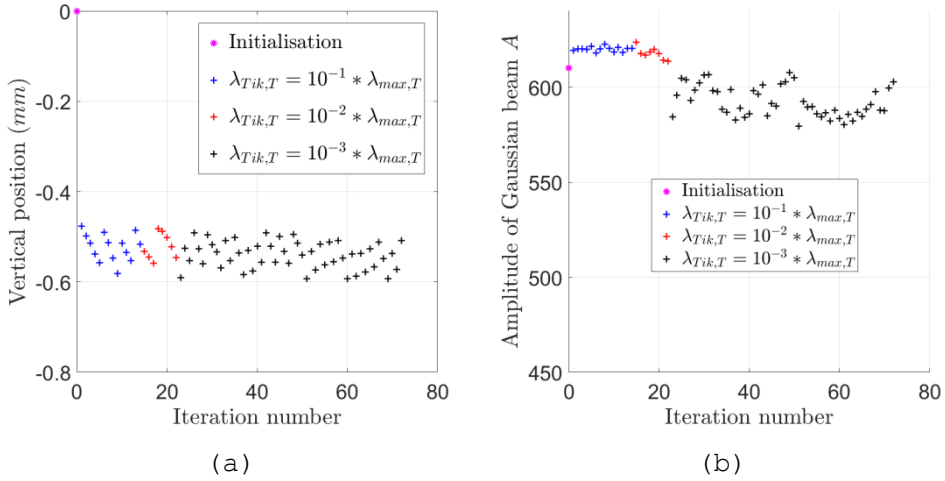

(a) (b)

Figure 20: Change of (a) Y position and (b) the amplitude of the laser loading during the iterative procedure for the first loading step

Residual fields at convergence are plotted in Figure 21 for the three heating steps. If the first step exhibits low residuals over the entire sample surface, the second and third steps show higher residuals in the center of the laser beam as the maximum temperature is underestimated and in the neighboring zone the temperature is overestimated (the dark ring around the red dot). Even if the relative difference is globally low, Figure 21(b) and (c) suggest that the residuals can be lowered in the central area, assuming this pattern is not only due to modeling errors. It is worth noting that the center of the sample is the most important area, as it will have consequences on the thermomechanical identification, particularly on the creep parameters. For this reason, the minimization has been conducted only on the central area (indicated by the box in Figure 21(b)) for the last two steps.

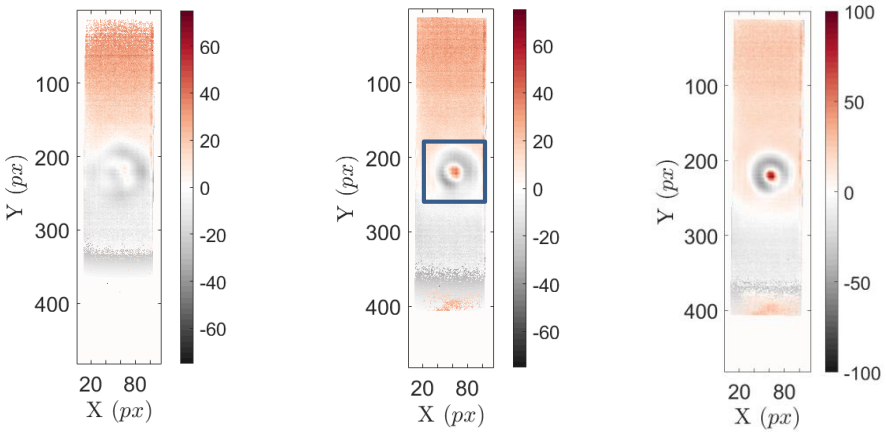

FIGURE 21: Residual fields (°C) considering minimization on the entire sample for (a) the first, (b) second and (c) last step. The blue box shows the central area where a second FEMU analysis will be run

Residual fields are plotted for these same steps in Figure 22. Even if there still is a similar pattern on the heated area, the maximum computed temperature is very close to the measured data (see Figure 23 in which the temporal evolution of five points located on and around the maximum temperature are plotted). Residuals are now lower in the heated area and acceptable given the range of temperature. However, it is recognized that there still are nonuniform residuals in the central area, which may be due to model errors.

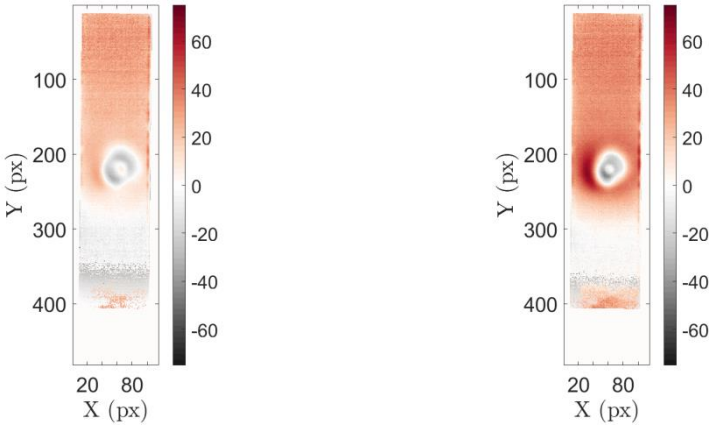

FIGURE 22: Residual fields (°C) considering the minimization on the central area (see Figure 21(b)) for (a) the second and (b) last steps

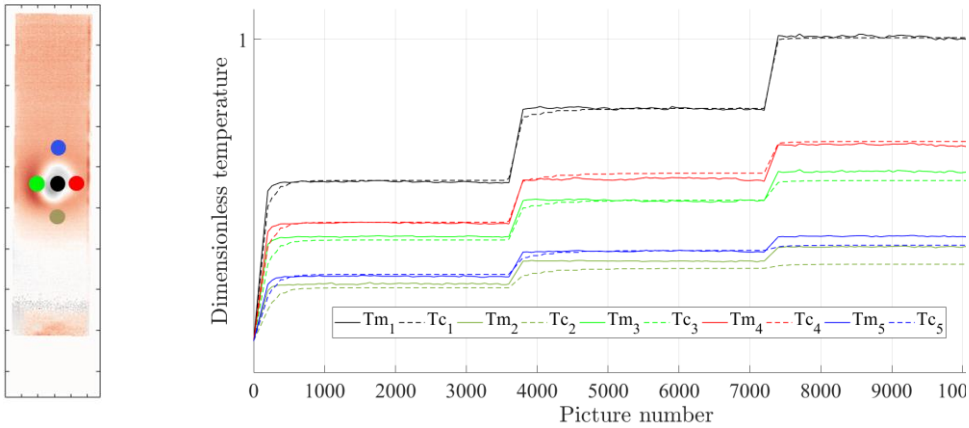

FIGURE 23: Comparison of thermal histories between computation and experiment for five points located in the central zone

5.2 Mechanical identification

In this section, the mechanical identification procedure is conducted for the two cases described in the previous section; first, the thermal identification has been performed on the entire sample, and second on the central area. For the first case, the change of the RMS residual is

plotted in Figure 24(a) with a decrease of 8%. It is worth noting that only the first two Tikhonov relaxations were considered because the increment of parameter vector did not converge during the third relaxation (Figure 24(b)). Although the RMS residual decreases afterward, the results are considered more trustworthy after the second relaxation.

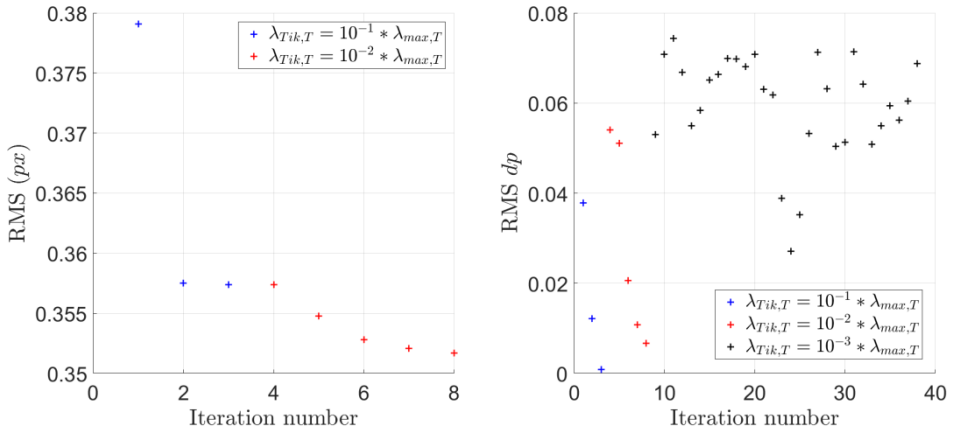

(a) (b)

FIGURE 24: Root mean square (a) displacement residual (px) and (b) increment of parameter history during the minimization procedure

An example of parameter change is shown in Figure 25 with the coefficient of the thermal expansion (CTE) and the creep stress exponent n. As for the thermal identification and according to the Hessian matrix (Figure 15(a)), the most sensitive parameter (the offset to the CTE) is adjusted first and, in this case, does not change hereafter. The creep stress exponent remains almost constant at the end of the first Tikhonov relaxation but increases at the end of the second relaxation. The reached value is consistent with high stress conditions, particularly at high temperatures [50].

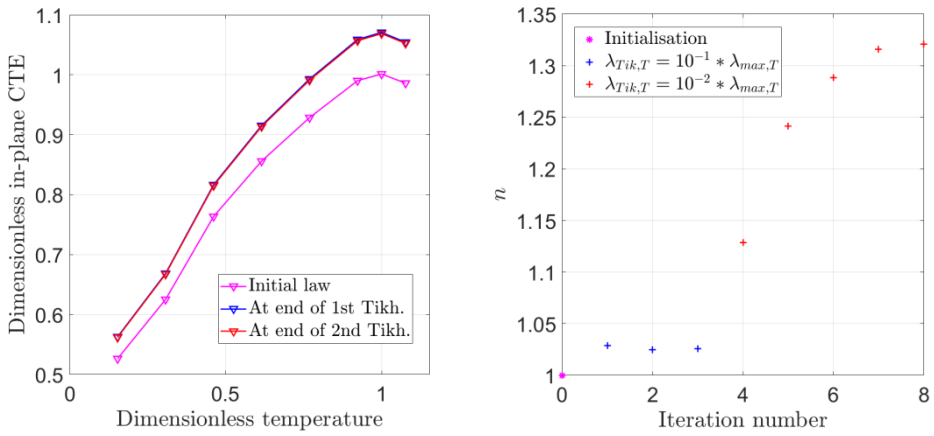

(a) (b)

FIGURE 25: Change of (a) coefficient of thermal expansion law and (b) creep stress exponent $\boldsymbol{n}$ with the iteration number and Tikhonov relaxation

The mechanical identification is conducted again, but this time with the temperature identification made on the central area. The RMS residual (Figure 26(a)) decrease is very close to the previous one with a lower final value (0.33 vs. $0.35\,px$). For the same reason (Figure 26(b)), the results are also taken after the second Tikhonov relaxation.

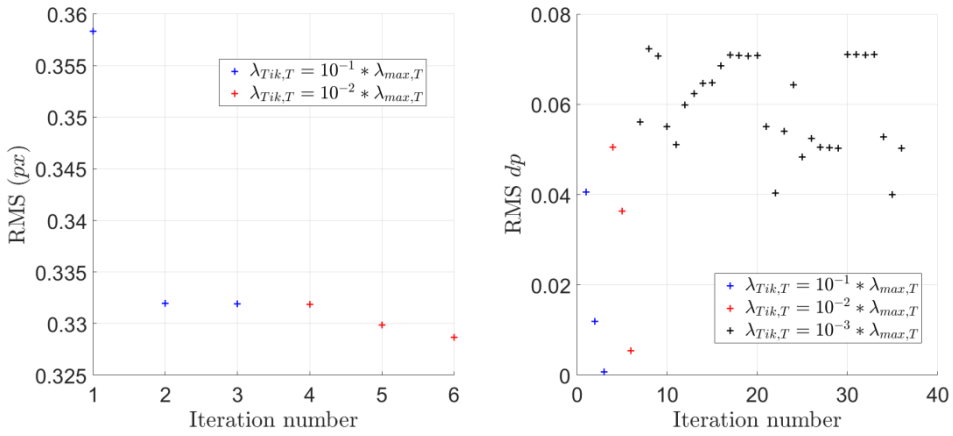

(a) (b)

FIGURE 26: Root mean square (a) displacement residual (px) and (b) increment of parameter history

Figure 27 shows the change of the same parameters during the calibration procedure on the central area. Both take very close values during the whole identification even if the calibrated creep stress exponent n is slightly closer to 1. This result proves the robustness of the procedure as the number of iterations is very close to the first case and the identified values too. Because the RMS residual is lower and the maximum computed temperatures are closer to the measured ones, comparisons on the displacements fields are made for the second case in the sequel.

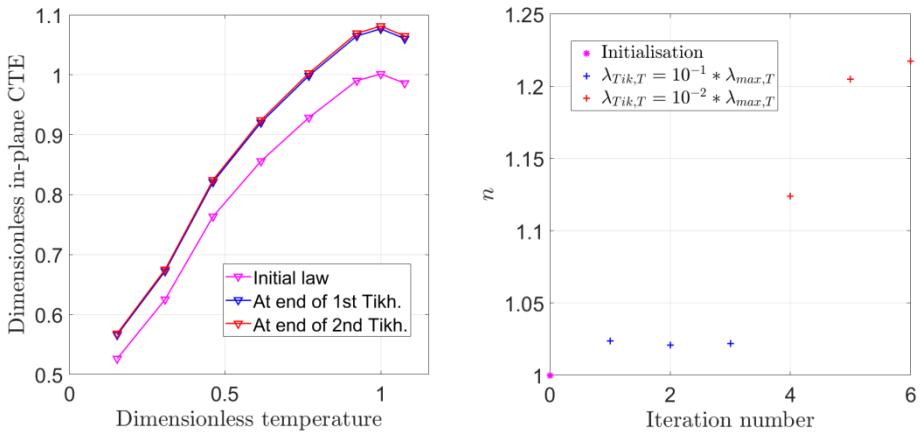

(a) (b)

FIGURE 27: Change of (a) coefficient of thermal expansion law and (b) creep law stress exponent $\boldsymbol{n}$

This case is interesting as the two sought parameters each have a major influence on one displacement component. As show in Figure 12(a) and Figure 13(a), creep parameters have very little influence on the elongation, which is however directly linked to the CTE. Conversely, Figure 12(b) and Figure 13(b) prove creep to be significantly influent on the deflection fields. Therefore, discussions on creep parameters are only made on the transerve displacements.

Figure 28 shows the deflection at the end of the sample before and after identification compared to DIC measurements. The updated creep parameters reduce the gap between measurements and modeling, with different values as those calibrated during TMA tests. The small remaining difference concerns the beginning of the step, when the temperature field is not stabilized. It can be linked with temperature differences in the transient stage. However, the thermal calibration procedure could also take into account material properties such as diffusivity, which are relevant when trying to reduce the gap in transient stages.

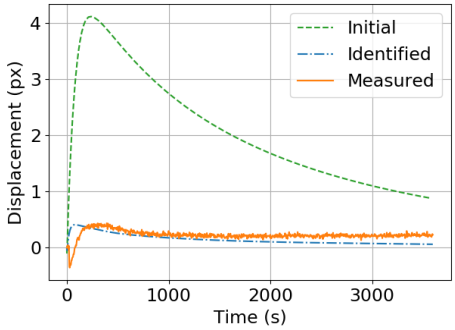

FIGURE 28: Deflection at the end of the sample obtained by DIC (solid line), for the initial and calibrated computation

Figure 29 shows the residual fields during the three stabilized heating steps. First, the RMS value of the residuals is respectively 0.12, 0.13 and $0.12\,px$ for the three heating steps, which is very low given the range of temperatures. As shown in Figure 8(b), most of the transverse displacement is on the right side of the sample, after the laser beam (located about $x = 1000\,px$). In this part, the residual levels are quite low for every step, about $0.2\,px$, which is also acceptable.

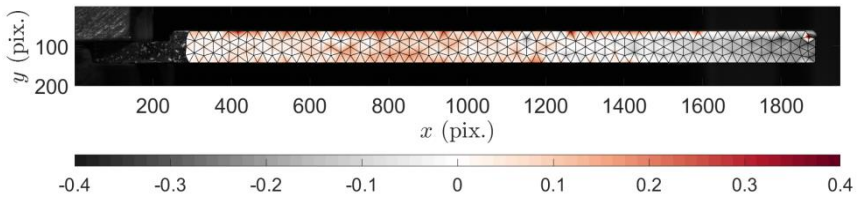

(a) RMS = 0.12 px

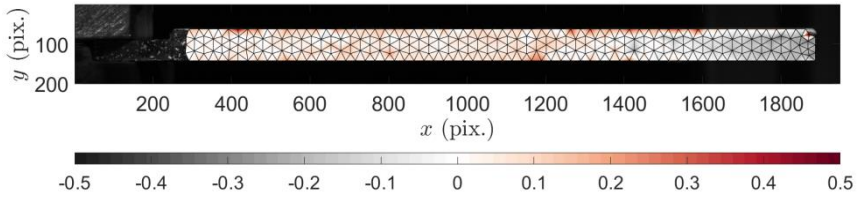

(b) RMS = 0.13 px

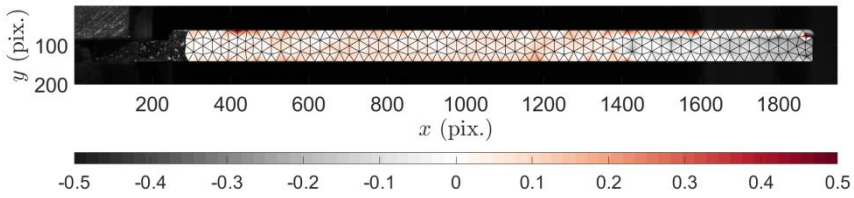

(c) RMS = 0.12 px

FIGURE 29: Residual displacement fields after identification in the transverse direction for the three stabilized heating steps

Table 4 summarizes the creep parameters used for initialization and obtained using FEMU. The time exponent m remains almost constant despite several differences in materials but also testing conditions, namely the loading, which is either tensile or compressive, and the stress level, which is higher using the laser test. Further, the stress exponent n calibrated with both FEMU cases tends to increase but remains close to 1, which is usually attributed to diffusion creep in ceramics [50], possibly with diffusional mass transport along the grain boundaries [51] that could be consistent with the microstructure of the coating.

TABLE 4: Creep parameters before and after the FEMU-T, FEMU-U procedures

Creep parameters	Initialization	FEMU-T on the entire surface	FEMU-T on the central zone
n	0.9	1.32	1.22
m	0.78	0.8	0.79

To assess the CTE change, Figure 30 shows the deflection at the end of the sample before and after identification compared to the DIC measurement for the first step. As already shown in Figure 25(a), in which the CTE increased after identification, residuals are slightly higher after the procedure, which was not expected. To explain this result, two hypotheses are proposed. First, the CTE sensitivity is too low to be properly identified with this procedure and this test. As only a small part of the sample is heated and only three heating steps are performed, it is the best case to identify a law written over a very large temperature range, particularly for ceramic materials whose CTE is low. Second, the uncoupled identification procedure may not be optimal, especially for this parameter, which is directly dependent on the temperature field. One possible solution would be to use a *FEMU-TU* procedure for this parameter and then a *FEMU-U* for the creep parameters. Uncertainties on the measured temperature field may also explain this result, especially for lower temperatures for which the IR camera is less sensitive.

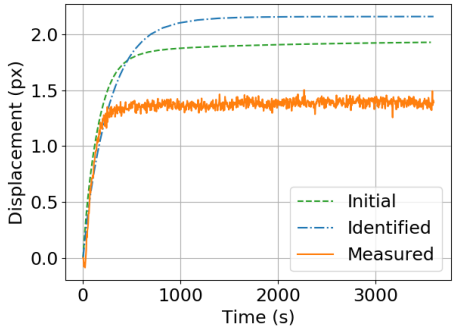

Figure 30: Elongation at the end of the sample obtained by DIC (solid line), for the initial and updated computation

6 Conclusion and perspectives

This paper proposed an experimental set-up to evaluate the thermomechanical behavior of an environmental barrier coating in conditions representative of turbine engine environments (i.e with thermal gradients). First, full-field measurements were conducted in challenging conditions, namely (1) true temperature fields with large thermal gradients required the knowledge of the emissivity and were essential to assess the thermal loading, (2) DIC measurements were successfully performed to measure small displacements (from 200 µm down to only a few tens of micrometers) at high temperatures with low uncertainties (about 1 µm).

These measurements were then compared to finite element models of the test to confirm that thermoelasticity was not sufficient to describe the material behavior. Moreover, the accuracy of the measurements allowed the investigated test to be sensitive to creep as there were large residuals between measured and computed deflections with the initial set of creep parameters.

In order to calibrate these parameters, an uncoupled weighted FEMU-T/FEMU-U framework was followed. The identication strategy was selected using a sensitivity

analysis and the study of the Hessian matrix, which revealed to be a valuable tool for test/computation correlations. Thus, the approach aimed to minimize weighted least squares residuals between measured and computed fields, first regarding temperatures to identify the thermal boundary conditions then kinematic data to assess thermomechanical parameters.

Furthermore, the results after thermal identification showed low residuals on the temperature fields and different results depending on the area of minimization. In both cases, the mechanical identification ended up with creep parameters in which the stress exponent was close to 1, which is consistent with diffusional creep observed in ceramic materials [50]. This observation shows the possibility to assess the creep behavior of the coating using full-field measurements combined with laser heating, which has the advantage of being sensitive to a range of temperatures and loadings with only one test. However, because of a globally low sensitivity given the challenging environment, thermomechanical parameters such as the coefficient of thermal expansion were not successfully identified with the chosen procedure and set of parameters.

Concerning the creep parameter identification, other constitutive postulates could be tested. For instance, creep stress and time exponents were considered independent of the temperature. In some cases at high temperatures, this choice may not be valid [14]. Thus, more tests would be required to assess this dependence.

Regarding the full identification procedure, the first step would be to increase the amplitude of displacements. In that case, it could be performed at the two endpoints of the sample by multiscale image correlation [52]. The right side because it is the most sensitive area for both elongation and deflection, and the left side because the kinematic boundary conditions close to the grips should be

measured as accurately as possible. Another possible route to improve the calibration could be to perform more tests with only one heating step at the same temperature but with several laser beam shapes to assess the effect of thermal loading and temperature level separately on the creep properties. The sensitivity analysis performed herein would help to design the best (i.e., most sensitive) loading history.

7 Acknowledgement

The authors would like to thank Dr. Manon Fernandez for her help and advice in this work, which was supported under PRC MECACOMP, a French research project co-funded by DGAC and SAFRAN Group, managed by SAFRAN Group and involving SAFRAN Group, ONERA and CNRS.

8 References

[1] M. P. Boyce, *Gas turbine engineering handbook*. Elsevier, 2011.

[2] P. P. Walsh et P. Fletcher, *Gas turbine performance*, 2nd ed. Malden, MA: Blackwell Science, 2004.

[3] A. G. Evans et D. B. Marshall, « The mechanical behavior of ceramic matrix composites », *Acta Metall.*, vol. 37, n° 10, p. 2567-2583, 1989.

[4] J. A. DiCarlo, H.-M. Yun, G. N. Morscher, et R. T. Bhatt, « SiC/SiC Composites for 1200°C and Above », in *Handbook of Ceramic Composites*, N. P. Bansal, Éd. Springer US, p. 77-98, 2005.

[5] G. N. Morscher *et al.*, « Tensile creep and fatigue of Sylramic-iBN melt-infiltrated SiC matrix composites: Retained properties, damage development, and failure mechanisms », *Compos. Sci. Technol.*, vol. 68, n° 15-16, p. 3305-3313, 2008.

[6] E. J. Opila, J. L. Smialek, R. C. Robinson, D. S. Fox, et N. S. Jacobson, « SiC Recession Caused by SiO_2 Scale Volatility under Combustion Conditions: II, Thermodynamics and Gaseous-Diffusion Model », *J. Am. Ceram. Soc.*, vol. 82, n° 7, p. 1826–1834, 1999.

[7] R. C. Robinson et J. L. Smialek, « SiC recession caused by SiO_2 scale volatility under combustion conditions: I, experimental results and empirical model », *J. Am. Ceram. Soc.*, vol. 82, n° 7, p. 1817–1825, 1999.

[8] M. J. Verrilli, E. J. Opila, A. Calomino, et J. D. Kiser, « Effect of Environment on the Stress-Rupture Behavior of a Carbon-Fiber-Reinforced Silicon Carbide Ceramic Matrix Composite », *J. Am. Ceram. Soc.*, vol. 87, n° 8, p. 1536-1542, 2004.

[9] K. N. Lee *et al.*, « Upper Temperature Limit of Environmental Barrier Coatings Based on Mullite and BSAS », *J. Am. Ceram. Soc.*, vol. 86, n° 8, p. 1299-1306, 2003.

[10] K. N. Lee, D. S. Fox, et N. P. Bansal, « Rare earth silicate environmental barrier coatings for SiC/SiC composites and Si_3N_4 ceramics », *J. Eur. Ceram. Soc.*, vol. 25, n° 10, p. 1705-1715, 2005.

[11] D. Zhu et R. A. Miller, « Influence of High Cycle Thermal Loads on Thermal Fatigue Behavior of Thick Thermal Barrier Coatings », *NASA Tech. Pap. TP-3676 Army Lab. Tech. Rep. ARL-TR-1341*, 1997.

[12] D. Zhu et R. A. Miller, « Determination of creep behavior of thermal barrier coatings under laser imposed high thermal and stress gradient conditions », *J. Mater. Res.*, vol. 14, n° 01, p. 146-161, 1998.

[13] D. Zhu et R. A. Miller, « Sintering and creep behavior of plasma-sprayed zirconia- and hafnia-based thermal

barrier coatings », *Surf. Coat. Technol.*, vol. 108-109, p. 114-120, 1998.
[14] G. Thurn, « High-temperature deformation of plasma-sprayed ZrO_2 thermal barrier coatings », *Mater. Sci. Eng. A*, vol. 233, n° 1-2, p. 176-182, 1997.
[15] B. P. Johnsen, T. A. Cruse, R. A. Miller, et W. J. Brindley, « Compressive Fatigue of a Plasma Sprayed ZrO_2-8wt%Y_2O_3 and ZrO_2-10wt%NiCrAlCoY TTBC », *J. Eng. Mater. Technol.*, vol. 117, p. 305, 1995.
[16] S. Avril *et al.*, « Overview of Identification Methods of Mechanical Parameters Based on Full-field Measurements », *Exp. Mech.*, vol. 48, n° 4, p. 381-402, 2008.
[17] Michel Grédiac et F. Hild, *Full-field measurements and identification in solid mechanics*. Jonh Wiley & Sons, 2012.
[18] K. T. Kavanagh et R. W. Clough, « Finite element applications in the characterization of elastic solids », *Int. J. Solids Struct.*, vol. 7, n° 1, p. 11-23, 1971.
[19] E. Pagnacco, A.-S. Caro-Bretelle, et P. Ienny, « Parameter Identification from Mechanical Field Measurements using Finite Element Model Updating Strategies », in *Full-Field Measurements and Identification in Solid Mechanics*, M. Grédiac, F. Hild, et A. Pineau, Éd. Hoboken, NJ USA: John Wiley & Sons, Inc., p. 247-274, 2012.
[20] R. Gras, H. Leclerc, S. Roux, S. Otin, J. Schneider, et J.-N. Périé, « Identification of the Out-of-Plane Shear Modulus of a 3D Woven Composite », *Exp. Mech.*, vol. 53, n° 5, p. 719-730, 2013.
[21] F. Mathieu, H. Leclerc, F. Hild, et S. Roux, « Estimation of Elastoplastic Parameters via Weighted FEMU and Integrated-DIC », *Exp. Mech.*, vol. 55, n° 1, p. 105-119, 2015.
[22] R. Gras, H. Leclerc, F. Hild, S. Roux, et J. Schneider, « Identification of a set of macroscopic elastic parameters in a 3D woven composite: Uncertainty analysis and regularization », *Int. J. Solids Struct.*, vol. 55, p. 2-16, 2015.
[23] B. T. Richards, L. J. Ghosn, D. Zhu, et H. N. G. Wadley, « Mechanical properties of air plasma sprayed environmental barrier coating (EBC) systems: preliminary assessments », *Proceedings of the 39th International Conference and Exposition on Advanced Ceramics and Composites*, 2015.
[24] B. Siebert, C. Funke, R. Vaβen, et D. Stöver, « Changes in porosity and Young's Modulus due to sintering of plasma sprayed thermal barrier coatings », *J. Mater. Process. Technol.*, vol. 92-93, p. 217-223, 1999.

[25] N. E. Massa *et al.*, « High temperature emissivity, reflectivity, and x-ray absorption of BiFeO3 », *J. Appl. Phys.*, vol. 108, n° 8, p. 084114, 2010.
[26] L. del Campo *et al.*, « High-Temperature Radiative Properties of an Yttria-Stabilized Hafnia Ceramic: High Temperature Radiative Properties of an YSH Ceramic », *J. Am. Ceram. Soc.*, vol. 94, n° 6, p. 1859-1864, 2011.
[27] C. Rodiet, « Mesure de Température par Méthodes Multi-Spectrales et Caractérisation Thermique de Matériaux Anisotropes par Transformations Intégrales:«Aspects Théoriques et Expérimentaux» », PhD Thesis, Université de Lorraine, 2014.
[28] M. A. Sutton, J. J. Orteu, et H. Schreier, *Image correlation for shape, motion and deformation measurements: basic concepts, theory and applications*. Springer Science & Business Media, 2009.
[29] J. S. Lyons, J. Liu, et M. A. Sutton, « High-temperature deformation measurements using digital-image correlation », *Exp. Mech.*, vol. 36, n° 1, p. 64–70, 1996.
[30] B. Pan, D. Wu, Z. Wang, et Y. Xia, « High-temperature digital image correlation method for full-field deformation measurement at 1200 C », *Meas. Sci. Technol.*, vol. 22, n° 1, p. 015701, 2010.
[31] B. M. B. Grant, H. J. Stone, P. J. Withers, et M. Preuss, « High-temperature strain field measurement using digital image correlation », *J. Strain Anal. Eng. Des.*, vol. 44, n° 4, p. 263-271, 2009.
[32] P. Leplay, O. Lafforgue, et F. Hild, « Analysis of Asymmetrical Creep of a Ceramic at 1350°C by Digital Image Correlation », *J. Am. Ceram. Soc.*, vol. 98, n° 7, p. 2240-2247, 2015.
[33] M. D. Novak et F. W. Zok, « High-temperature materials testing with full-field strain measurement: Experimental design and practice », *Rev. Sci. Instrum.*, vol. 82, n° 11, p. 115101, 2011.
[34] A. Charbal *et al.*, « Integrated Digital Image Correlation considering gray level and blur variations: Application to distortion measurements of IR camera », *Opt. Lasers Eng.*, vol. 78, p. 75-85, 2016.
[35] A. Maynadier, M. Poncelet, K. Lavernhe-Taillard, et S. Roux, « One-shot Measurement of Thermal and Kinematic Fields: InfraRed Image Correlation (IRIC) », *Exp. Mech.*, vol. 52, n° 3, p. 241-255, 2012.
[36] A. Mendoza, J. Schneider, E. Parra, E. Obert, et S. Roux, « Differentiating 3D textile composites: A novel field of application for Digital Volume Correlation », *Compos. Struct.*, vol. 208, p. 735-743, 2019.
[37] G. Besnard, H. Leclerc, F. Hild, S. Roux, et N. Swiergiel, « Analysis of image series through global digital image correlation », *J. Strain Anal. Eng. Des.*, vol. 47, n° 4, p. 214-228, 2012.

[38] M. Berny, T. Archer, A. Mavel, P. Beauchêne, S. Roux, et F. Hild, « On the analysis of heat haze effects with spacetime DIC », *Opt. Lasers Eng.*, vol. 111, p. 135-153, 2018.
[39] Y. L. Dong et B. Pan, « A Review of Speckle Pattern Fabrication and Assessment for Digital Image Correlation », *Exp. Mech.*, vol. 57, n° 8, p. 1161-1181, 2017.
[40] T. Archer, P. Beauchêne, C. Huchette, et F. Hild, « Global digital image correlation up to very high temperatures with grey level corrections », *Meas. Sci. Technol.*, vol. 31, 024003, 2019.
[41] Z. Tomičevć, F. Hild, et S. Roux, « Mechanics-aided digital image correlation », *J. Strain Anal. Eng. Des.*, vol. 48, n° 5, p. 330-343, 2013.
[42] H. Leclerc, J. Neggers, F. Mathieu, F. Hild, et S. Roux, « Correli 3.0, IDDN. FR. 001.520008. 000. SP 2015.000. 31500 », *Agence pour la Protection des Programmes Paris (France)*, 2015.
[43] Y. Jannot, « Transferts thermiques », *Ecole des mines de Nancy (France)*, 2012.
[44] G. Dusserre, F. Nazaret, L. Robert, et T. Cutard, « Applicability of image correlation techniques to characterise asymmetric refractory creep during bending tests », *J. Eur. Ceram. Soc.*, vol. 33, n° 2, p. 221-231, 2013.
[45] L. Massard, « Etude du fluage de réfractaires électrofondus du système alumine-zircone-silice », PhD Thesis, Ecole Nationale Supérieure de Mines de Paris, 2005.
[46] E. P. Simoncelli, « Bayesian Multi-Scale Differential Optical Flow », in *Handbook of Computer Vision and Applications*, vol. 2, Academic Press, p. 297–422, 1999.
[47] A. Tarantola, *Inverse Problems Theory. Methods for Data Fitting and Model Parameter Estimation*. Southampton (UK): Elsevier Applied Science, 1987.
[48] F. Hild et S. Roux, « Comparison of Local and Global Approaches to Digital Image Correlation », *Exp. Mech.*, vol. 52, n° 9, p. 1503-1519, 2012.
[49] G. Besnard, F. Hild, et S. Roux, « "Finite-Element" Displacement Fields Analysis from Digital Images: Application to Portevin–Le Châtelier Bands », *Exp. Mech.*, vol. 46, n° 6, p. 789-803, 2006.
[50] A. H. Chokshi et T. G. Langdon, « Characteristics of creep deformation », vol. 7, p. 8, 1991.
[51] R. L. Coble, « A Model for Boundary Diffusion Controlled Creep in Polycrystalline Materials », *J. Appl. Phys.*, vol. 34, n° 6, p. 1679-1682, 1963.
[52] J.-C. Passieux, F. Bugarin, C. David, J.-N. Périé, et L. Robert, « Multiscale Displacement Field Measurement Using Digital Image Correlation: Application to the

Identification of Elastic Properties », *Exp. Mech.*, vol. 55, n° 1, p. 121-137, 2015.